Mean Shift-Based Defect Detection in Multicrystalline Solar Wafer Surfaces

Du-Ming Tsai and Jie-Yu Luo

***Abstract*—This paper presents an automated visual inspection scheme for multicrystalline solar wafers using the mean-shift technique. The surface quality of a solar wafer critically determines the conversion efficiency of the solar cell. A multicrystalline solar wafer contains random grain structures and results in a heterogeneous texture in the sensed image, which makes the defect detection task extremely difficult.**

Mean-shift technique that moves each data point to the mode of the data based on a kernel density estimator is applied for detecting subtle defects in a complicated background. Since the grain edges enclosed in a small spatial window in the solar wafer show more consistent edge directions and a defect region presents a high variation of edge directions, the entropy of gradient directions in a small neighborhood window is initially calculated to convert the gray-level image into an entropy image. The mean-shift smoothing procedure is then performed on the entropy image to remove noise and defect-free grain edges. The preserved edge points in the filtered image can then be easily identified as defective ones by a simple adaptive threshold. Experimental results have shown the proposed method performs effectively for detecting fingerprint and contamination defects in solar wafer surfaces.

***Index Terms*—Defect detection, machine vision, mean shift, multicrystalline solar wafer, surface inspection.**

I. Introduction

IMAGE analysis techniques have been used extensively for visual surface inspection to ensure product quality and production yield in manufacturing. Surface defect detection algorithms are generally developed for uniform or homogeneously textured surfaces, where local anomalies that break the visual homogeneity from their surrounding background are identified as defects. The surface defect detection task is classified as qualitative inspection [1] which involves detecting ill-defined, nonquantifiable faulty items such as scratches, cracks, stain and wear. In this paper, we focus on defect detection in a multicrystalline solar wafer that contains a heterogeneously textured surface in the image.

Defects on uniform/nontextured surfaces such as glass [2] and sheet steel [3] can be effectively detected using simple thresholding or edge detection techniques if the defects in these uniform images have distinct pixel values with respect to those of the background. For textured surface inspection, texture analysis techniques [4] have been widely used to tackle the defect detection problem. A set of texture features extracted from the spatial domain or from the spectral domain are generally used as discrimination measures, and then a classifier in high dimensional space such as Bayes probability [5], maximum likelihood [6] or neural networks [7] is applied to distinguish defective regions from the background pattern. The texture features are calculated from a small neighborhood window that slides over the entire image in a pixel-by-pixel basis. It assumes that the texture patterns enclosed in the neighborhood window show the same similarity everywhere in the image, and is only applicable to homogeneously textured surfaces.

In spatial-domain approaches, the commonly used texture features are the second-order statistics derived from spatial gray-level co-occurrence matrices [8]. They have been applied to wood inspection [9], carpet wear assessment [10], roughness measurement of machined surfaces [11], and textile defect detection [12].

In spectral-domain approaches, texture features are popularly derived from the power spectra using Fourier transforms [13], [14]. They have been successively applied to fabric defect detection [15], [16] and patterned wafer inspection [17] in the semiconductor industry. In the recent past, multiresolution decomposition schemes based on wavelet transforms [18], [19] have been an attractive alternative for texture feature extraction. The multiresolution wavelet representation allows an image to be decomposed into a hierarchy of local subimages at different spatial frequencies [20]. The texture features are then extracted from the decomposed subimages in different frequency channels and different resolution levels. They have been applied to the inspection of LSI wafers [21], fabrics [22]–[24], and homogeneously textured surfaces [25].

Filtering techniques using the joint spatial/spatial-frequency Gabor transforms [26]–[28] are also commonly used to design a filter bank that represents the characteristics of the textured patterns. They have been applied to the inspection of wooden surfaces [29], granite [30], steel surfaces [31], and textile fabrics [32]–[34]. Kumar and Pang [35] used a set of finite impulse response filters for defect detection in textiles. The optimal filters were selected based on discriminant analysis from defect-free and defective regions in training images. Xie and Mirmehdi [36] generated a set of texture exemplars by exploring a Gaussian mixture model from defect-free image patches, and used them for defect detection on ceramic tiles. The abnormality is measured by the likelihood of each patch in the inspection image. A low likelihood indicates a possible defect region.

A homogeneously textured surface generally presents repetitive, periodical patterns in the image. Therefore, the self-similarity property can be easily used as a cue for defect detection. The local feature extraction and filtering techniques described

Manuscript received May 04, 2010; revised July 26, 2010; accepted October 15, 2010. Date of publication December 10, 2010; date of current version February 04, 2011. Paper no. TII-10-05-0109.

The authors are with Yuan-Ze University, Industrial Engineering and Management, Tao-Yuan 330, Taiwan (e-mail: iedmtsai@saturn.yzu.edu.tw; s965415@mail.yzu.edu.tw).

Color versions of one or more of the figures in this paper are available online at http://ieeexplore.ieee.org.

Digital Object Identifier 10.1109/TII.2010.2092783

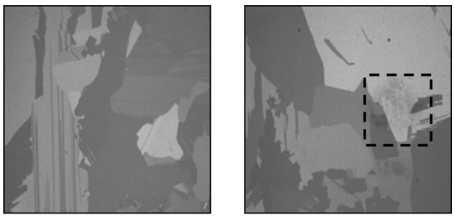

(a) (b)

Fig. 1. Two sample images of multicrystalline solar wafers. (a) Defect-free multigrain wafer surface. (b) Defective wafer surface containing a fingerprint defect.

previously only perform well for defect detection in uniform and homogeneously textured surfaces. For heterogeneously textured surfaces, similar patterns will not repeatedly appear in the image. It makes the discrimination between faultless and defective regions extremely difficult.

In semiconductor manufacturing, a wafer contains repeated dies of the same electrical components and layout. The defect detection algorithms for wafer die inspection utilize the property that all dies in the wafer show identical patterns. Die-to-die comparison [37] between adjacent dies in the wafer is a simple method to detect the difference. A collection of defect-free dies are used as the golden template [38], or are used as the training samples in neural networks [39] for comparison or classification. Self-reference methods [40]–[42] that generate the template from the inspection wafer itself are also used for wafer die inspection. The repetitive periods in both horizontal and vertical directions are first evaluated. A synthetic template is then created from the image itself based on the pixel values in subsequent periods, and is used for comparison with the inspection image. Shankar and Zhong [43] proposed alternatively a nonreferential method based on wavelet decomposition and morphological operations for wafer die inspection. It requires a specific design of structuring elements for individual defect types and assumes that local defects and any parts of the background are structurally different. Since each multicrystalline solar wafer has a unique pattern and local defects could be structurally similar to crystal grain edges, the currently available defect inspection algorithms for patterned wafers cannot be extended for defect detection in multigrain solar wafers.

Solar power is an attractive alternative of electrical energy due to growing environmental concern and oil shortage. Multicrystalline, instead of monocrystalline, material dominates the production volume of silicon cells owing to lower manufacturing costs. Fig. 1(a) shows the image of a defect-free multicrystalline solar wafer surface. It contains multiple grains of random shapes and sizes and, therefore, results in a heterogeneously textured pattern. There are no two solar wafers with the same grain patterns. Fig. 1(b) displays a defective solar wafer image that contains a fingerprint defect marked by a dotted frame in the image. It can be seen from the figure that the defect is very difficult to identify from the heterogeneous background. The conventional defect detection methods for uniform and homogeneous surfaces are not directly extensible for defect detection in multicrystalline solar wafers that involve heterogeneous surfaces.

Mean shift is a nonparametric feature space analysis tool that finds the modes in multiple-dimensional data using kernel density estimators. The mean-shift algorithm was first introduced by Fukunaga and Hostetler [44] for nonparametric clustering of vector-valued data. It is extended to image processing by Comaniciu and Meer [45]. It has been successfully applied to edge-preserving smoothing [46], [47], image segmentation [48], [49], and texture segmentation/ classification [50], [51].

In image processing applications, the mean-shift algorithm shifts each pixel with pixel coordinates and pixel value as the features to the mode. Since flat regions induce the modes, it can be expected that a noisy background can be effectively smoothed while the meaningful edges can be preserved. In this study, the defect detection scheme based on mean-shift smoothing is proposed for multicrystalline solar wafer inspection.

The fingerprint and contamination embedded in multicrystalline solar wafers are the main defect types evaluated in this study. Detecting defects in the original gray-level image is impossible because both defects and the multigrain background present similar gray-level distributions. Since the grain edges enclosed in a small spatial window in the multicrystalline silicon wafer show more consistent edge directions and a defective region presents a high variation of edge directions, the entropy of gradient directions in the spatial window is first calculated to convert the gray-level image into an entropy image. The mean-shift smoothing procedure is then performed to remove noise and defect-free grain edges in the entropy image. The suspected edge points in the filtered image are identified as defective ones by using a simple adaptive threshold. The goal of the proposed algorithm is to detect the presence/absence of defects in a solar wafer image. The detected defects will be presented in a binary image to visualize the detection results. However, accurate segmentation of defect positions, shapes, and sizes is out of the scope of this study.

This paper is organized as follows. Section II first overviews the mean-shift algorithm. The proposed defect detection scheme for solar wafer images with heterogeneous textures is then presented. The section ends with the guidelines and automatic parameter setting for the choice of mean-shift kernel bandwidths. Section III presents the experimental results on multicrystalline solar wafers. The effect of changes in parameter values of the mean-shift procedure is also evaluated in this section. This paper is concluded in Section IV.

II. Defect Detection Using Mean Shift

For the sake of completeness, this section starts with the overview of the mean-shift algorithm proposed by Comaniciu and Meer [45], followed by the proposed defect detection scheme for solar wafer surfaces with heterogeneous textures.

A. Mean Shift Algorithm

Given a set of N data points $\boldsymbol{x}_i, i = 1, 2, \ldots, N$, and $\boldsymbol{x}_i \in \Re^d$, the probability density of $\boldsymbol{x}$ can be obtained from the kernel density estimator

$$p(\boldsymbol{x}) = \frac{1}{N} \sum_{i=1}^{N} K(\boldsymbol{x} - \boldsymbol{x}_i). \tag{1}$$

The kernel $K(\boldsymbol{z})$ is generally given by a uniform function

$$K_U(\boldsymbol{z}) = \begin{cases} c, & \text{if } \|\boldsymbol{z}\| \leq 1 \\ 0, & \text{otherwise} \end{cases} \tag{2}$$

or by a Gaussian function

$$K_G(\boldsymbol{z}) = c \cdot \exp\left(-\frac{1}{2}\|\boldsymbol{z}\|^2\right). \tag{3}$$

In practice, the kernel $K(\boldsymbol{z})$ uses the form

$$K(\boldsymbol{z}) = c \cdot k(\|\boldsymbol{z}\|) \tag{4}$$

where $k(\|\boldsymbol{z}\|)$ is called the profile of the kernel, and c is a normalization constant.

Since the dense regions in the feature space correspond to the local maxima of the probability density function, the gradient of the density function can be obtained from the estimate of the density gradient. Hence

$$\nabla p(\boldsymbol{x}) = \frac{1}{N}\sum_{i=1}^{N} \nabla K(\boldsymbol{x} - \boldsymbol{x}_i). \tag{5}$$

By using the kernel form

$$K(\boldsymbol{x} - \boldsymbol{x}_i) = c \cdot k\left(\left\|\frac{\boldsymbol{x} - \boldsymbol{x}_i}{h}\right\|^2\right)$$

the gradient of the density function becomes

$$\begin{aligned} \nabla p(\boldsymbol{x}) &= \frac{c}{N}\sum_{i=1}^{N} \nabla k\left(\left\|\frac{\boldsymbol{x} - \boldsymbol{x}_i}{h}\right\|^2\right) \\ &= \frac{c}{N}\left[\sum_{i=1}^{N} g\left(\left\|\frac{\boldsymbol{x} - \boldsymbol{x}_i}{h}\right\|^2\right)\right] \\ &\quad \cdot \left[\frac{\sum_{i=1}^{N} \boldsymbol{x}_i \cdot g\left(\left\|\frac{\boldsymbol{x}-\boldsymbol{x}_i}{h}\right\|^2\right)}{\sum_{i=1}^{N} g\left(\left\|\frac{\boldsymbol{x}-\boldsymbol{x}_i}{h}\right\|^2\right)} - \boldsymbol{x}\right] \end{aligned} \tag{6}$$

where $g(\|\boldsymbol{x} - \boldsymbol{x}_i/h\|^2) = -k'(\|\boldsymbol{x} - \boldsymbol{x}_i/h\|^2)$, and h is the bandwidth to adjust the resolution for the difference between $\boldsymbol{x}$ and $\boldsymbol{x}_i$. The difference between the weighted mean and the center of the kernel is called "mean shift," i.e.,

$$\boldsymbol{m}(\boldsymbol{x}) = \frac{\sum_{i=1}^{N} \boldsymbol{x}_i \cdot g\left(\left\|\frac{\boldsymbol{x}-\boldsymbol{x}_i}{h}\right\|^2\right)}{\sum_{i=1}^{N} g\left(\left\|\frac{\boldsymbol{x}-\boldsymbol{x}_i}{h}\right\|^2\right)} - \boldsymbol{x}. \tag{7}$$

The mean-shift vector always points to the direction of maximum increment in the density. The mean-shift algorithm moves iteratively each data point $\boldsymbol{x}$ in the feature space by the mean-shift vector $\boldsymbol{m}(\boldsymbol{x})$ until the mean converges to an estimate of the local mode of the data set.

In image processing applications, a pixel $\boldsymbol{x}$ of an image is a data point represented by the two-dimensional pixel coordinates $\boldsymbol{x}^s = (x, y)$ in the spatial domain and the pixel values $\boldsymbol{x}^r$, such as gray-level or RGB color features, in the range domain. The kernel $K(\cdot)$ is defined as the product of the spatial profile $k_s(\cdot)$ and the range profile $k_r(\cdot)$

$$K(\boldsymbol{x}) = c \cdot k_s\left(\left\|\frac{\boldsymbol{x}^s}{h_s}\right\|\right) \cdot k_r\left(\left\|\frac{\boldsymbol{x}^r}{h_r}\right\|\right) \tag{8}$$

where h_s is the spatial bandwidth for feature vector $\boldsymbol{x}^s$ and h_r is the range bandwidth for feature vector $\boldsymbol{x}^r$. A common profile $k(\cdot)$ is usually used for $k_s(\cdot)$ and $k_r(\cdot)$ in both domains.

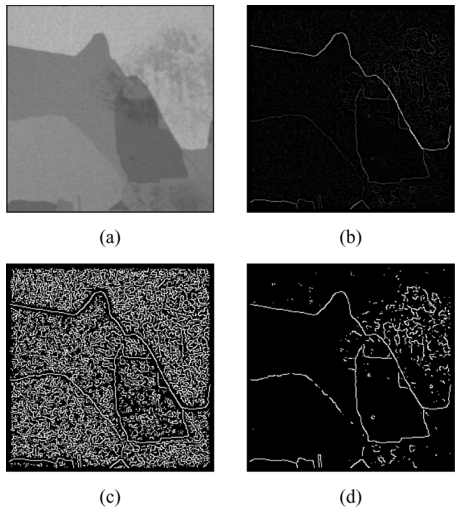

Fig. 2. Gradient images of a defective solar wafer. (a) Defective solar wafer image. (b) Gradient image of (a). (c) Binarization result of (b) with a tight gradient threshold. (d) Binarization result of (b) with a loose gradient threshold.

B. Proposed Multicrystalline Solar Wafer Inspection Scheme

A multicrystalline solar wafer shows random multi-grain textures in the image. The grain patterns are different from wafer to wafer. No two wafers have the same patterned surfaces. The conventional mean-shift filtering that works on the gray-level image cannot remove all the grains and preserve only anomalies in the smoothed image since the multigrain background and the defects show no gray-level difference. The mean-shift segmentation can only best divide each grain in the solar wafer into individual region, and does not provide any direct cue for defect detection.

There are various types of defects found on multicrystalline solar wafers such as cracks, holes, oil stains, and fingerprints. Different defect types may need different detection strategies for the inspection. In this study, we especially aim at the defects of fingerprints and contamination. By closely observing the solar wafer images in Fig. 1, one can find that the edges between crystal grains are clear and sharp. The grain edges in a small spatial window show only a few direction changes. However, the intrusion objects on the silicon wafer generally do not present sharp edges. A fingerprint or a contamination defect involves many smaller disjointed regions and present blurred edges. Fig. 2(a) demonstrates a sample solar wafer that contains a fingerprint on the upper-right portion of the image. The fingerprint does not show clear edges and consistent edge directions.

Since the gray levels in the original wafer image do not provide sufficient information for the discrimination between defective and defect-free regions, the entropy of gradient directions of all edge points in a small neighborhood window is first calculated to convert the gray-level image into an entropy image. A defect-free region presents more consistent edge directions and results in a small entropy value. A defective region shows a high variation of edge directions and yields a large entropy value. The mean-shift filtering is then proceeded in the entropy image to remove noise and smooth defect-free grain edges. A simple adaptive threshold can then be applied to distinguish defective edge points from the background points in the filtered entropy image.

1) Conversion of Direction Entropy: Let $e(x, y)$ be an edge point, which is detected by the Canny edge detector [52] in this study. Fig. 2(b) shows the gradient image of the defective solar wafer in Fig. 2(a). Fig. 2(c) and (d) display the detected edges as binary images for Fig. 2(b) with a small gradient threshold (a gradient magnitude of 10) and a large gradient threshold (a gradient magnitude of 40), respectively. The results show that the defect region cannot be simply identified from the gradient image.

The gradient direction for an edge point $e(x, y)$ with its original gray-level $f(x, y)$ is given by

$$\theta(x, y) = \tan^{-1}\left(\frac{\Delta y}{\Delta x}\right) \tag{9}$$

where $\Delta x = f(x+1, y) - f(x-1, y)$; $\Delta y = f(x, y+1) - f(x, y-1)$. The gradient angle $\theta(x, y)$ is further extended in the range between 0° and 360° by considering the signs of Δx and Δy.

Denote by $p(\theta_i)$ the probability of gradient angle θ in interval i in a small neighborhood window. In this study, the histogram of gradient angles is divided into 100 intervals and the neighborhood window is of size 19×19 pixels. The entropy of gradient directions for each edge point $e(x, y)$ in a small neighborhood window is defined as

$$E(x, y) = -\sum_i p(\theta_i) \cdot \log p(\theta_i). \tag{10}$$

The entropy $E(x, y)$ of a non-edge point is set to zero. Now the original gray-level image $f(x, y)$ is converted to an entropy image $E(x, y)$.

Fig. 3(a) shows the solar wafer image containing a fingerprint defect, in which square A marks a defect-free region and square B marks a portion of the fingerprint. Fig. 3(b) and (c) present, respectively, the histograms of gradient angles for squares A and B. Due to the horizontal grain edges in square A, the gradient histogram of square A is more concentrated at 90°, whereas the gradient angles are more uniformly distributed in all directions for square B. These result in an entropy of 3.56 for the defect-free region of square A, and 4.09 for the defective region of square B. Fig. 3(d) and (e) further depict the gradient angles of squares A and B in 3D perspective. A simple thresholding cannot be directly applied to the entropy image to distinguish the difference between defect-free and defective regions.

2) Mean-Shift Filtering for Grain Edge Removal: In order to remove the noisy points generated from the grain edges in the entropy image, the mean-shift filtering is performed on the entropy image. The mean-shift process assigns a background value (i.e., the mode) to the normal grain edges, while preserving the entropy values of defective edges. A simple adaptive threshold based on the mean and standard deviation of entropy values in the whole filtered image is then used for identifying the defective points from the background in the image. In this study, the simple uniform kernel is used in the mean-shift procedure. The Gaussian kernel generates similar detection results. The proposed mean-shift scheme for defect detection in solar wafer surfaces with heterogeneous textures is expressed in detail as follows.

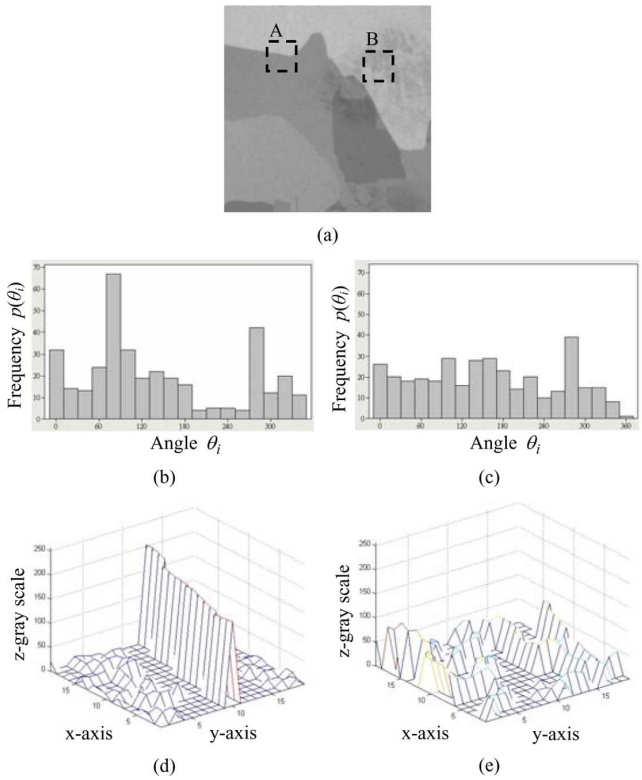

Fig. 3. Distributions of gradient angles in defect-free and defective regions of a solar wafer: (a) solar wafer image, where dotted frame A is defect-free and dotted frame B contains a portion of the fingerprint; (b), (c) histograms of gradient angles for defect-free region A and defective region B, respectively; (d), (e) plots of gradient angles in 3D perspective for regions A and B, respectively.

Algorithm:

Input: $f(x, y) =$ image of size $M \times N$ to be inspected
$h_s =$ spatial bandwidth
$h_r =$ range (entropy) bandwidth
$T_\varepsilon =$ termination threshold of the mean-shift iterations

Step 1. Convert the gray-level image $f(x, y)$ into the entropy image $E(x, y)$, for $x = 0, 1, 2, \ldots, M-1$ and $y = 0, 1, 2, \ldots, N-1$ using (9) and (10).

Step 2. Perform the mean-shift filtering on the entropy image $E(x, y)$ pixel by pixel, for $x = 0, 1, 2, \ldots, M-1$ and $y = 0, 1, 2, \ldots, N-1$. For each pixel (x, y), find the converged location (x^*, y^*). Replace the entropy value $E(x, y)$ with $E(x^*, y^*)$. It iterates as follows.

Step 2a. Assign the kernel center.
Let

$$x_c^t = x_w^{t-1}$$
$$y_c^t = y_w^{t-1}$$
$$f_c^t = f_w^{t-1}$$

where $x_w^0 = x$, $y_w^0 = y$ and $f_w^0 = E(x,y)$;
t is the current iteration number with an initial value of one; (x_c^t, y_c^t) is the current center of the kernel.
Step 2b. Compute the kernel weight of pixel (x,y) within the spatial window defined by h_s

$$w\left(x_c^t + i, y_c^t + j\right) = \begin{cases} 1, & \text{if } \left|E\left(x_c^t + i, y_c^t + j\right) - f_c^t\right| \le h_r \\ 0, & \text{otherwise} \end{cases}$$

for all $i^2 + j^2 \le h_s^2$.
Step 2c. Update the weighted mean

$$x_w^t = \frac{1}{S_w} \sum_{i,j} w\left(x_c^t + i, y_c^t + j\right) \cdot \left(x_c^t + i\right)$$
$$y_w^t = \frac{1}{S_w} \sum_{i,j} w\left(x_c^t + i, y_c^t + j\right) \cdot \left(y_c^t + j\right)$$
$$f_w^t = \frac{1}{S_w} \sum_{i,j} w\left(x_c^t + i, y_c^t + j\right) \cdot E\left(x_c^t + i, y_c^t + j\right)$$

where $S_w = \sum_{i,j} w\left(x_c^t + i, y_c^t + j\right)$.
Step 2d. Calculate the mean shift ε^t

$$\varepsilon^t = (\Delta x^t)^2 + (\Delta y^t)^2 + (\Delta f^t)^2$$

where

$$\Delta x^t = x_w^t - x_c^t$$
$$\Delta y^t = y_w^t - y_c^t$$
$$\Delta f^t = f_w^t - f_c^t.$$

If $\varepsilon^t > T_\varepsilon$, then let $t = t + 1$ and repeat steps 2*a*–*d* until it is converged.
Otherwise, let , $(x^*, y^*) = (x_w^t, y_w^t)$,

$$E(x,y) = f_w^t.$$

Step 3. Identify defect points in the filtered image by a simple adaptive threshold. The entropy threshold is given by the statistical control limit, and is defined as

$$\mu_E + C_E \cdot \sigma_E$$

where μ_E and σ_E are the mean and standard deviation of the whole filtered entropy image, and C_E is a control constant. If $E(x,y) > (\mu_E + C_E \cdot \sigma_E)$, then pixel (x,y) is a defective point. Otherwise, it is classified as a defect-free point.

Fig. 4(a1) and (b1) show the gray-level images of a defect-free wafer and a defective one, respectively. Fig. 4(a2) and (b2) are the corresponding entropy images of Fig. 4(a1) and (b1), where the brightness is proportional to the entropy magnitude. Fig. 4(a3) and (b3) are the smoothed entropy images after mean-shift filtering. The filtering results

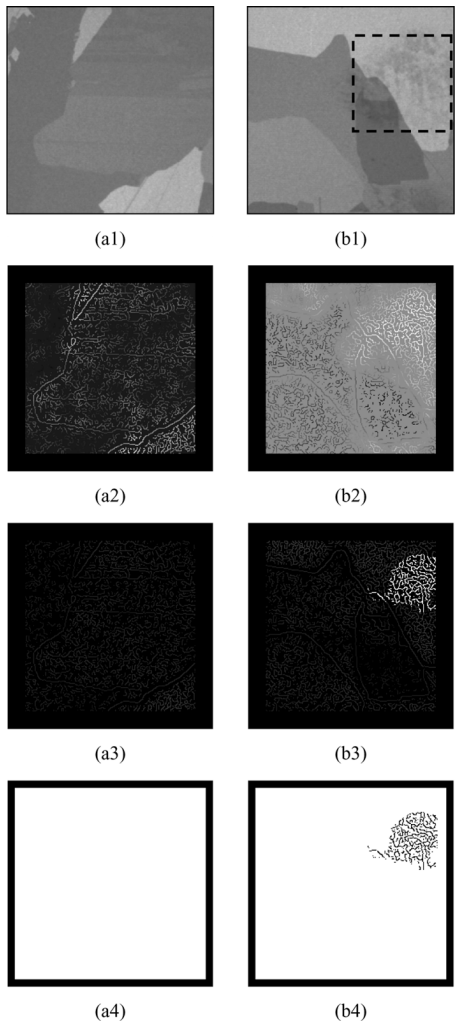

Fig. 4. Solar wafer surface inspection using the proposed defect detection scheme: (a1) defect-free solar wafer image; (b1) defective solar wafer image; (a2), (b2) entropy images $E(x,y)$ of (a1) and (b1), respectively; (a3), (b3) respective smoothed results of (a2) and (b2) after mean-shift filtering; (a4), (b4) corresponding binarization results of (a3) and (b3) with threshold $\mu_E + 4 \cdot \sigma_E$.

show that the entropy values in the normal grain regions are effectively smoothed, and the entropy values in the fingerprint region is distinctly highlighted. The threshold results are shown as binary images in Fig. 4(a4) and (b4). The fingerprint region is well identified, and no defect points are declared in the defect-free solar wafer.

C. Choice of Mean-Shift Parameter Values

The most difficult task in the use of mean-shift filtering is the choice of parameter values for spatial bandwidth h_s, range bandwidth h_r and the termination threshold T_ε. The spatial bandwidth h_s determines the spatial window for the neighboring pixels to consider. It is relatively easy to choose based on the geometric requirement. In the entropy image of a solar wafer, the noisy background cannot be sufficiently smoothed if the selected spatial window is too small. A small h_s value is computationally more efficient. The computation load increases as the h_s value increases.

The termination threshold T_ε of the mean-shift process is based on the mean-shift magnitude in the feature space in two consecutive iterations. That is

$$(\Delta x)^2 + (\Delta y)^2 + (\Delta f)^2$$

where Δx and Δy are related to the spatial bandwidth and Δf is associated with the range (entropy) bandwidth h_r. The termination threshold is therefore adaptively expressed as a function of h_s and h_r. Once the spatial bandwidth h_s and the range bandwidth h_r are determined, it is given by

$$T_\varepsilon = P \cdot h_s \cdot h_r \tag{11}$$

where P is a percentage constant between 0% and 100%.

Among the three parameters h_s, h_r, and T_ε, the most critical one is the range bandwidth h_r for defect detection applications. Rather than trial-and-error, a more systematic approach is required for automatic selection of a proper range bandwidth for specific surfaces. In defect detection applications, an h_r value larger than the maximum difference of feature values will cause no false positive points in a defect-free surface. Therefore, the number of noisy points will decrease as the range bandwidth increases. However, an excessively large h_r value reduces the discrimination power to identify the defect points. In this study, the range bandwidth h_r is automatically learned from a set of defect-free test samples. The objective is to find a minimum range bandwidth under the constraints that all defect-free test images generate no noisy points. Let I_i, $i = 1, 2, \ldots, n$, be a set of n defect-free test images. The optimization model for range bandwidth selection is formulated as

$$\begin{aligned} \text{Min} \quad & h_r \\ \text{s.t.} \quad & E_i(x,y) < \mu_{E_i} + C_{E_i} \cdot \sigma_{E_i} \\ & \text{for all } (x,y) \text{ and } i = 1, 2, \ldots, n \end{aligned} \tag{12}$$

where $E_i(x,y)$ is the entropy of gradient directions for pixel (x,y) in test image I_i.

Generally, the possible values of h_r are limited in a very small range. An exhaustive search with a given resolution can be easily carried out to find the optimal value of h_r. In this study, the range bandwidth is associated with the entropy. A small resolution of 0.1 is used to find the best h_r value. The selected h_r value from the optimization model achieves a best discrimination power for defect detection, while maintaining the stability for defect-free samples.

III. Experimental Results

In this section, we present experimental results on a number of heterogeneous solar wafer surfaces. The proposed algorithms are implemented on a Pentium Core2 Duo, 3.0 GHz personal computer using the C++ language. The test images are 256×256 pixels wide with 8-bit gray levels. The spatial resolution of the image is 0.09 mm per pixel. The mean computation time is 2.0 s for a 256×256 solar wafer image. In order to demonstrate the effectiveness of the proposed methods, no smoothing preprocessing is applied to the input gray-level images and no morphological postprocessing is used to remove noise and connect blobs in the resulting binary images. In Sections III-A–III-E, the effects of changes in parameter values of h_s, h_r, T_ε, and neighborhood window size are separately evaluated.

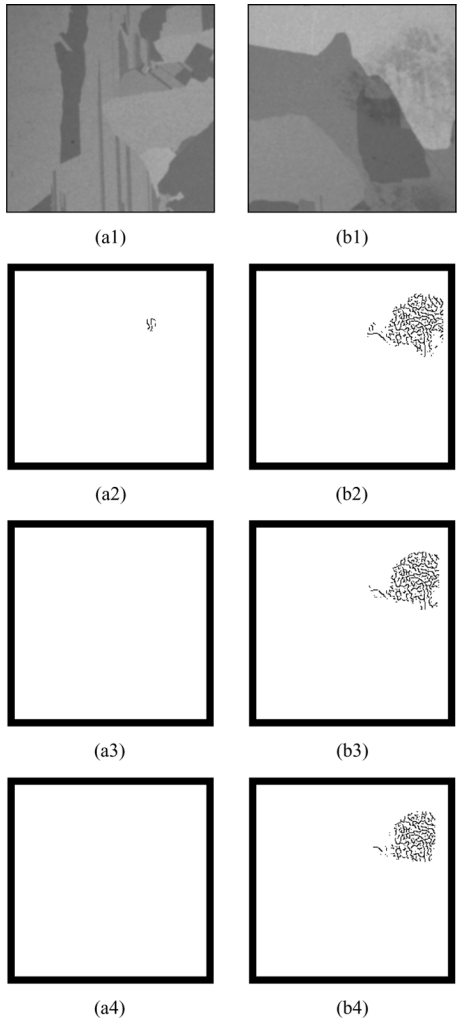

Fig. 5. Effect of changes in spatial bandwidth h_s on solar wafer surfaces: (a1) defect-free solar wafer image; (b1) defective solar wafer image; (a2)–(a4) detection results with $h_s = 15$, 20 and 25 for the defect-free image in (a1); (b2)–(b4) detection results with the respective h_s values for the defective image in (b1). (a2) $h_s = 15$ (a3) $h_s = 20$ (a4) $h_s = 25$ (b2) $h_s = 15$ (b3) $h_s = 20$ (b4) $h_s = 25$.

A. Effect of Changes in Spatial Bandwidth h_s

The spatial bandwidth h_s determines the number of neighboring pixels used in the kernel. A small spatial bandwidth causes a fast convergence of the mean-shift process. The early termination of mean-shift filtering with a small h_s value may not sufficiently smooth the background and results in noisy points. A very large h_s value may oversmooth the entropy image and reduce the detected size of a defect.

Fig. 5(a1) and (b1) show a defect-free and a defective solar wafer image, respectively. Given that $h_r = 4.0$ (determined by the automatic h_r selection model), $P = 0.1\%$ for the termination threshold and $C_E = 4$ for the control limit, Fig. 5(a2)–(a4) and (b2)–(b4) present the detection results with varying spatial bandwidth values of $h_s = 15$, 20, and 25.

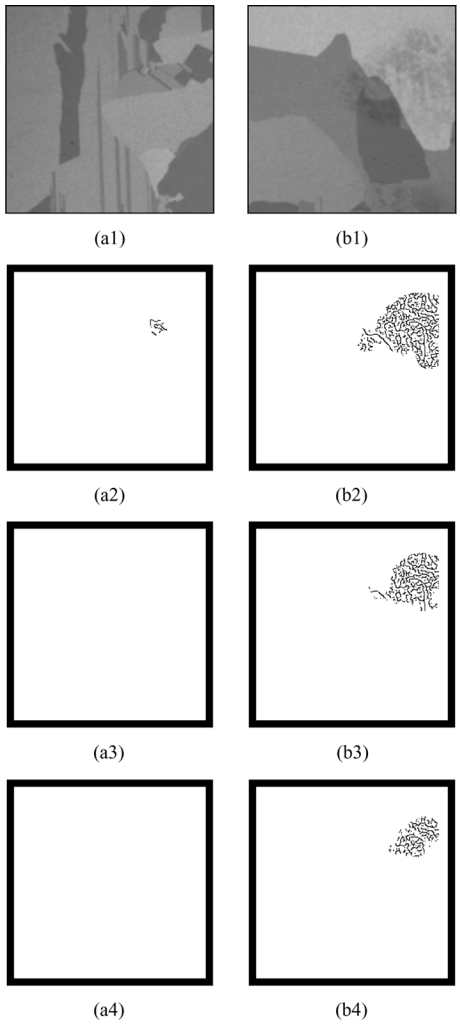

Fig. 6. Effect of changes in range bandwidth h_r on solar wafer surfaces: (a1) defect-free solar wafer image; (b1) defective solar wafer image; (a2)–(a4) detection results with $h_r = 3.9$, 4.0 and 4.1 for the defect-free image in (a1); (b2)–(b4) detection results with the respective h_r values for the defective image in (b1). (a2) $h_r = 3.9$ (a3) $h_r = 4.0$ (a4) $h_r = 4.1$ (b2) $h_r = 3.9$ (b3) $h_r = 4.0$ (b4) $h_r = 4.1$.

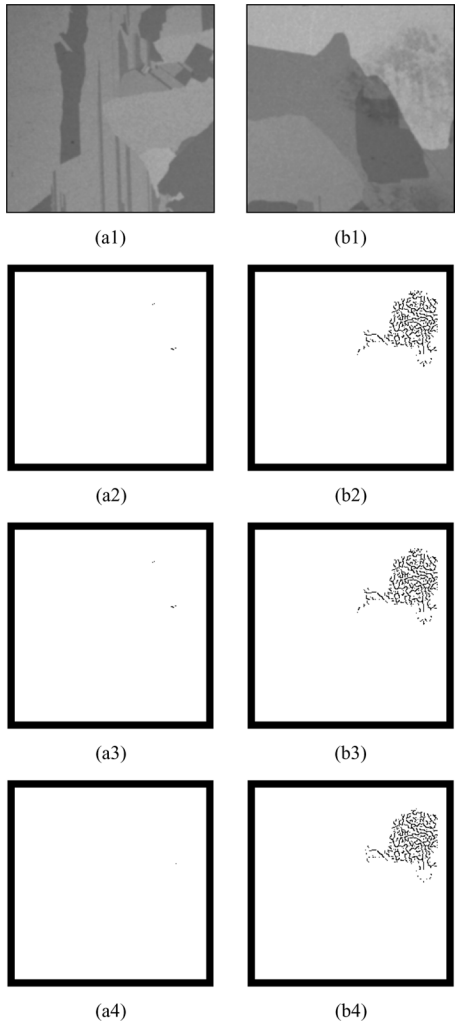

Fig. 7. Effect of changes in termination threshold T_ε on solar wafer surfaces: (a1) defect-free solar wafer image; (b1) defective image; (a2)–(a4) detection results with $P = 1\%$, 0.1% and 0.01% for the defect-free image in (a1); (b2)–(b4) detection results with the respective P values for the defective image in (b1). (a2) $P = 1\%$ (a3) $P = 0.1\%$ (a4) $P = 0.01\%$ (b2) $P = 1\%$ (b3) $P = 0.1\%$ (b4) $P = 0.01\%$.

The proposed inspection schemes are not sensitive to the changes in spatial bandwidth. The fingerprint defect is reliably detected, regardless of the h_s values in the experiment. A small spatial bandwidth generates some minor noisy points for the defect-free test images, as seen in Fig. 5(a2) with $h_s = 15$.

B. Effect of Changes in Range Bandwidth h_r

In this paper, we have proposed an automatic selection model to determine the best range bandwidth h_r^* for defect detection. In this section, the effect of varying range bandwidth in the neighborhood of h_r^* on the detection results is evaluated. The spatial bandwidth h_s is set to 20 based on the experimental results in Section III-A. All remaining parameters $P = 0.1\%$ and $C_E = 4$ are the same as those in the previous experiment.

Fig. 6(a1) and (b1) show the same defect-free and defective solar wafer images as those in Fig. 5(a1) and (b1). The range bandwidth of entropy varies with $h_r = 3.9$, 4.0 and 4.1, where $h_r^* = 4.0$ is the best range bandwidth given by the automatic selection model. The detection results in Fig. 6(a2)–(a4) and (b2)–(b4) show that the fingerprint defect can be reliably detected with various h_r values. A small range bandwidth generates a few isolated noisy points, as seen in Fig. 6(a2). A large range bandwidth reduces the actual size of the defect, as observed in Fig. 6(b4). The experimental results reveal that the range bandwidth is a critical factor for the success of defect detection, and the proposed automatic selection model can indeed choose a best h_r value for solar wafer inspection.

C. Effect of Changes in Termination Threshold T_ε

Mean shift is an iterative algorithm. One has to specify a termination criterion and check for the convergence of each pixel in the image. In this study, the termination threshold T_ε is adaptively given by a constant fraction of $h_s \cdot h_r$, i.e., $T_\varepsilon = P \cdot h_s \cdot h_r$, with $0\% < P < 100\%$. In this experiment, all the parameter values (spatial bandwidth h_s, range bandwidth h_r and control constant C_E) are chosen based on the best values found in Sections III-A and III-B.

Fig. 7 displays the detection results of the solar wafer images with $P = 1\%$, 0.1% and 0.01%. The resulting binary images

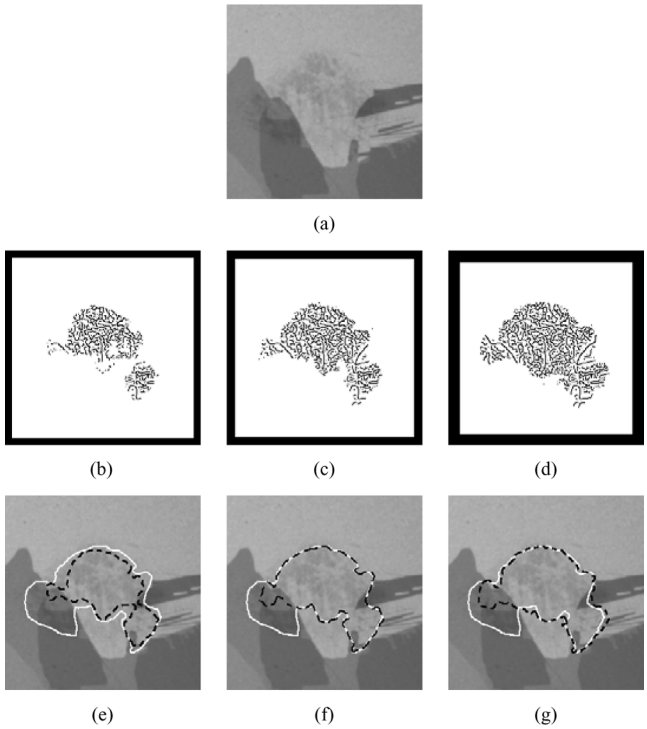

Fig. 8. Effect of changes in windows size for the computation of direction entropy: (a) fingerprint image for the test; (b)–(d) detected fingerprint regions with window sizes of 15×15, 19×19 and 23×23, respectively; (e)–(g) defect regions detected manually (solid-white lines for the ground truth region) and algorithmically (dotted-black lines). (b) 15×15 (c) 19×19 (d) 23×23.

indicate that the proposed mean-shift defect detection scheme are not sensitive to the changes of P value for the termination threshold T_ε. The P values in the range between 1% and 0.01% all generate similar detection results for solar wafer surfaces. The proposed termination threshold as a small percentage of $h_s \cdot h_r$ can effectively determine the required convergence for defect-free and defective pixels in the inspection image. A tight P value (e.g., $P = 0.01\%$) generally results in less noise, but induces more mean-shift iterations. A P value of 0.1% has generally performed well for various test surfaces, and is recommended for the mean shift-based defect detection scheme.

D. Effect of Changes in Window Sizes for Entropy Feature

In order to evaluate the effect of changes in the neighborhood window for the computation of direction entropy, the fingerprint image in Fig. 8(a) is used as the test sample, and the detection results with window sizes 15×15, 19×19, and 23×23 are presented in Fig. 8(b)–(d), respectively. All three window sizes can detect the fingerprint. A small neighborhood window tends to reduce the detected defect size, whereas a large neighborhood window enlarges the defect size and may generate noise. The effect of changes in window size is also analyzed with receiver operating characteristic curves in Section III-E.

To further verify the detected defect size with respect to the ground truth region, Fig. 8(e)–(g) shows the defect regions detected algorithmically and manually, where the solid-white lines are the ground-truth regions and the dotted-black lines are the detected regions. When the fingerprint is clear in the wafer surface, it can be well identified and the detected contour is consistent with the manually marked region. For the fingerprint lying between multiple grains regions, the print is light and is hardly visible. The proposed method thus misdetects this portion of the fingerprint.

E. More Testing Results

The efficacy of the proposed defect detection methods with the best parameter values found in the previous experiments is demonstrated with more solar wafer images. Fig. 9 shows a set of 8 multicrystalline solar wafers, where (a1)–(d1) are defect-free images, and (e1)–(f1) contain fingerprint defects and (g1)–(h1) present contamination defects. The detection result of Fig. 9(a1)–(h1) are shown as binary images in Fig. 9(a2)–(h2), respectively. The hardly identifiable defects in all defective test images are well segmented. The resulting binary images of defect-free test images are uniformly white and no defects are declared. The proposed method can be well applied to defect detection in solar wafer surfaces, where defects present high gradient direction variation with respect to the crystal grain edges.

In order to further verify the detection performance of the proposed method, a total of 130 test samples are evaluated. The test set contains 10 fingerprint samples, 20 contamination samples of various sizes, and 100 defect-free wafer images with random grain patterns. In the experiment, an image under test is declared as defective if there are any black pixels in the resulting binary image. Only the one with all white pixels in the entire binary image is claimed to be defect-free. Morphological operations could be carried out to eliminate noisy points in the binary image. However, the postprocessing operations are not applied in the experiment to show the robustness of the proposed algorithm. With the same parameter setting of $h_s = 20$, $h_r = 4.0$, $P = 0.1\%$ and $C_E = 4$, all the 30 defective images are correctly detected and the false negative rate is 0. Only one of the 100 defect-free images is falsely identified and the corresponding false positive rate is 1%. The receiver operating characteristic (ROC) curves of the proposed method for the 130 test samples are also evaluated. The proposed algorithm aims at the detection of presence/absence of defects in an image and, thus, the ROC curve is analyzed at the image level. Since the parameters h_s and P are insensitive to the detection results, we present only the ROC curves for varying range bandwidth h_r of 3.9, 4.0, and 4.1 in Fig. 10(a). For a given range bandwidth value, the ROC curve is constructed by varying the control constant C_E from a very small number (with a true positive rate of 1) to a very large number (with a false positive rate of zero). The ROC curve rises swiftly upward with $h_r = 4.0$ and indicates a very good performance of the proposed method.

Fig. 10(b) further shows the ROC curves of the proposed method for the 130 test images with varying window sizes of 15×15, 19×19, and 23×23. In the 30 defective images, the defect sizes range from 543 pixels (0.8% of the whole image area) to 13502 pixels (20% of the image). The window size of 19×19 gives the best performance. All the defects of varying sizes can be detected with this setting. A larger window size of 23×23 tends to have better performance than a smaller window size of 15×15.

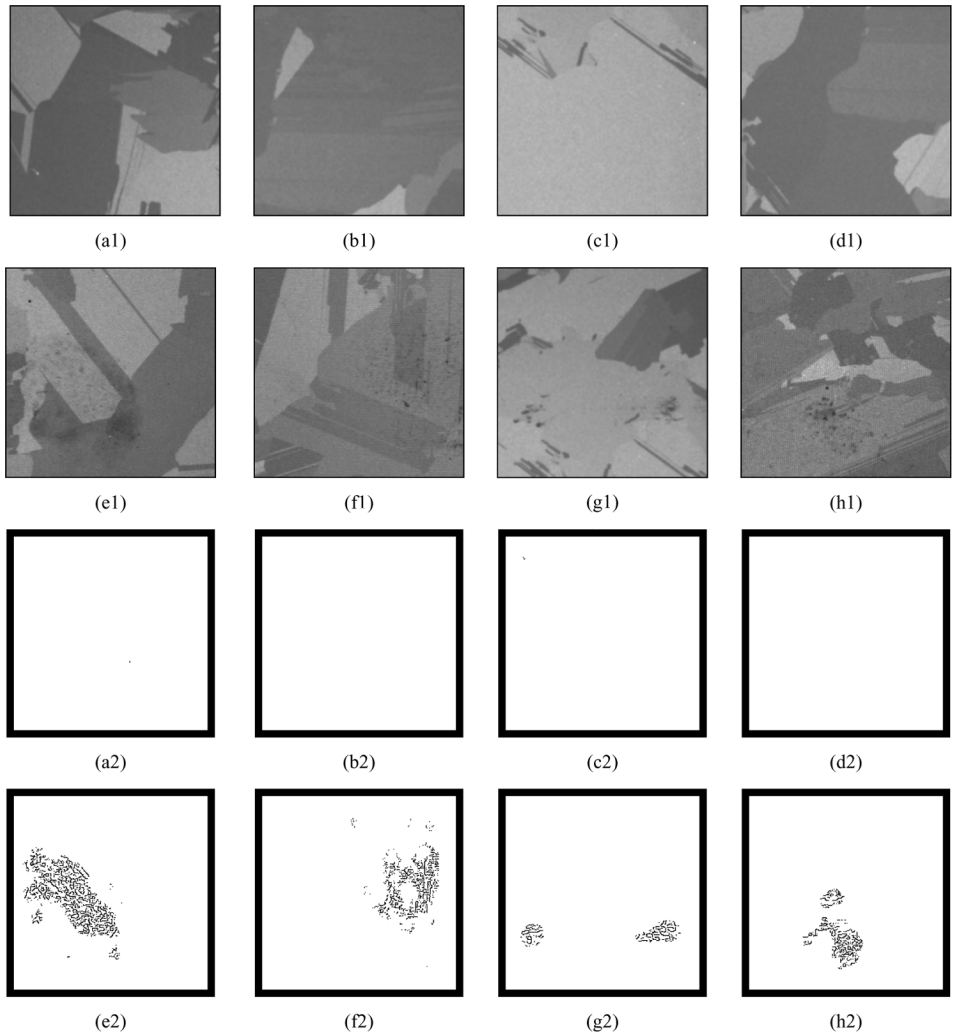

Fig. 9. Detection results of multicrystalline solar wafers: (a1)–(d1) four defect-free wafer images; (e1)–(f1) fingerprint images; (g1)–(h1) contamination images; (a2)–(h2) respective binarization results for wafer images in (a1)–(h1).

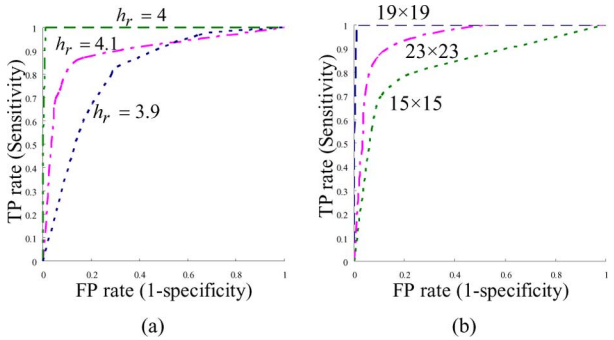

Fig. 10. ROC curves of the proposed method with (a) varying range bandwidth h_r and (b) varying window size for entropy computation.

IV. Conclusion

This paper has presented a mean shift-based machine vision method for detecting fingerprint and contamination defects in multicrystalline solar wafers. The defect types involve random gradient directions, whereas the normal grain edges generally present more consistent gradient directions in a small spatial window. The entropy of gradient directions is then used as the range feature. The pixel coordinates along with the entropy form the feature space of the image. The mean-shift smoothing can effectively remove noise and residuals of crystal grain edges and preserve only the defective pixels in the filtered image. A simple adaptive threshold can thus be used to segment the defective region in the filtered entropy image.

Currently, the mean computation time of the proposed method is 2.0 s for a 256×256 solar wafer image with a pure software implementation. A hard-wired implementation of the algorithm may be required for online inspection in manufacturing. The computation of the proposed algorithm mainly depends on the number of recursive mean-shift operations. The effective adjustment of spatial and range bandwidths under a given small number of mean-shift iterations should be further studied so that the computational load can be significantly reduced.

Experimental results have shown that the proposed defect detection scheme can perform well for identifying fingerprint and contamination in multicrystalline solar wafers. However, it is currently limited to the defect types that involve high gradient

direction variation. It cannot be directly extended to other defect types such as cracks that show only line-shaped figures and present a low variation in gradient directions. Different discrimination features may be needed for different types of defects to construct the vector-valued feature image. The proposed mean-shift process can then be applied to smooth the feature values in the background and retain the feature values of local anomalies. It is worthy of further investigation.

REFERENCES

[1] T. S. Newman and A. K. Jain, "A survey of automated visual inspection," *Computer Vision and Image Understanding*, vol. 61, pp. 231–262, Mar. 1995.

[2] J. Wilder, "Finding and evaluating defects in glass," in *Machine Vision for Inspection and Measurement*, H. Freeman, Ed. New York: Academic Press, 1989, pp. 237–237.

[3] J. Olsson and S. Gruber, "Web process inspection using neural classification of scattering light," in *Proc. IEEE Int. Conf. Ind. Electron., Control, Instrum. Autom.*, San Diego, CA, 1992, pp. 1443–1448.

[4] X. Xie, "A review of recent advances in surface defect detection using texture analysis techniques," *Electron. Lett. Computer Vision and Image Analysis*, vol. 7, pp. 1–22, 2008.

[5] D. Brzakovic, H. Beck, and N. Sufi, "An approach to defect detection in materials characterized by complex textures," *Pattern Recogn.*, vol. 23, pp. 99–107, 1990.

[6] F. S. Cohen, "Maximum likelihood unsupervised textured image segmentation," *CVGIP: Graphical Models Image Process*, vol. 54, pp. 239–251, 1992.

[7] M. M. Van Hulle and T. Tollenaere, "A modular artificial neural networks for texture processing," *Neural Networks*, vol. 6, pp. 7–32, 1993.

[8] R. M. Haralick, K. Shanmugam, and I. Dinstein, "Texture features for image classification," *IEEE Trans. Syst., Man, Cybernetics*, vol. 3, pp. 610–621, 1973.

[9] R. W. Conners, C. W. McMillin, K. Lin, and R. E. Vasquez-Espinosa, "Identifying and locating surface detects in wood," *IEEE Trans. Pattern Anal. Mach. Intell.*, vol. PAMI-5, pp. 573–583, 1983.

[10] L. H. Siew and R. M. Hogdson, "Texture measures for carpet wear assessment," *IEEE Trans. Pattern Anal. Mach. Intell.*, vol. 10, pp. 92–105, 1988.

[11] K. V. Ramana and B. Ramamoorthy, "Statistical methods to compare the texture features of machined surfaces," *Pattern Recogn.*, vol. 29, pp. 1447–1459, 1996.

[12] A. Bodnarova, J. Williams, M. Bennamoun, and K. Kubik, "Optimal textural features for flaw detection in textile materials," in *Proc. IEEE TENCON'97 Conf.*, Brisbane, Queensland, 1997, pp. 13–18.

[13] S. S. Liu and M. E. Jernigan, "Texture analysis and discrimination in additive noise, computer vision," *Graphics, Image Process*, vol. 49, pp. 52–67, 1990.

[14] R. Azencott, J. P. Wang, and L. Younes, "Texture classification using windowed Fourier filters," *IEEE Trans. Pattern Anal. Mach. Intell.*, vol. 19, no. 2, pp. 148–153, Feb. 1997.

[15] J. Escofet, M. S. Millan, H. Abril, and E. Torrecilla, "Inspection of fabric resistance to abrasion by Fourier analysis," in *Proc. SPIE*, Brugge, Belgium, 1998, vol. 3490, pp. 207–210.

[16] C.-H. Chan and K.-H. Pang, "Fabric defect detection by Fourier analysis," *IEEE Trans. Ind. Appl.*, vol. 36, no. 5, pp. 1267–1276, Sep./Oct. 2000.

[17] T. Ohshige, H. Tanaka, Y. Miyazaki, T. Kanda, H. Ichimura, N. Kosaka, and T. Tomoda, "Defect inspection system for patterned wafers based on the spatial-frequency filtering," in *Proc. IEEE/CHMT Eur. Int. Electronic Manuf. Technol. Symp.*, New York, 1991, pp. 192–196.

[18] S. G. Mallat, "A theory for multiresolution signal decomposition: The wavelet representation," *IEEE Trans. Pattern Anal. Mach. Intell.*, vol. 11, no. 7, pp. 674–693, Jul. 1989.

[19] T. Chen and C. C. J. Kuo, "Texture analysis and classification with tree-structured wavelet transform," *IEEE Trans. Image Processing*, vol. 2, no. 4, pp. 429–441, Oct. 1993.

[20] C. H. Chen and G. G. Lee, "On digital mammogram segmentation and microcalcification detection using multiresolution wavelet analysis," *Graphical Models Image Process*, vol. 59, pp. 349–364, 1997.

[21] K. Maruo, T. Shibata, T. Yamaguchi, M. Ichikawa, and T. Ohmi, "Automatic defect pattern detection on LSI wafers using image processing techniques," *IEICE Trans. Electronics*, vol. E82-C, pp. 1003–1012, 1999.

[22] H. Sari-Sarraf and J. Goddard, "Vision systems for on-loom fabric inspection," *IEEE Trans. Industry Applications*, vol. 35, no. 6, pp. 1252–1259, Nov./Dec. 1999.

[23] J. Scharcanski, "Stochastic texture analysis for monitoring stochastic processes in industry," *Pattern Recogn. Lett.*, vol. 26, pp. 1701–1709, 2005.

[24] X. Yang, G. Pang, and N. Yung, "Robust fabric defect detection and classification using multiple adaptive wavelets," *IEE Proc. Vision, Image Processing*, vol. 152, pp. 715–723, 2005.

[25] G. Lambert and F. Bock, "Wavelet methods for texture defect detection," in *Proc. IEEE Int. Conf. Image Process.*, Washington, DC, 1997, vol. 3, pp. 201–204.

[26] J. G. Daugman, "Uncertainty relation for resolution in space, spatial-frequency, and orientation optimized by two-dimensional visual cortical filters," *J. Opt. Soc. Amer.*, vol. 2, pp. 1160–1169, 1985.

[27] M. Clark and A. C. Bovik, "Texture segmentation using Gabor modulation/demodulation," *Pattern Recogn. Lett.*, vol. 6, pp. 261–267, 1987.

[28] D. A. Clausi and M. E. Jernigan, "Designing Gabor filters for optimal texture separability," *Pattern Recogn.*, vol. 33, pp. 1835–1849, 2000.

[29] W. Polzleitner and G. Schwingskakl, "Quality classification of wooden surfaces using Gabor filters and genetic feature optimization," in *Proc. SPIE*, Boston, MA, 1999, vol. 3837, pp. 220–231.

[30] G. Paschos, "Fast color texture recognition using chromaticity moments," *Pattern Recogn. Lett.*, vol. 21, pp. 837–841, 2000.

[31] K. Wiltschi, A. Pinz, and T. Lindeberg, "Automatic assessment scheme for steel quality inspection," *Mach. Vision Appl.*, vol. 12, pp. 113–128, 2000.

[32] A. Bodnarova, M. Bennamoun, and S. J. Latham, "Constrained minimization approach to optimize Gabor filters for detecting flaws in woven textiles," in *Proc. IEEE Int. Conf. Acoustics, Speech and Signal Processing*, Istanbul, Turkey, 2000, vol. 6, pp. 3606–3609.

[33] A. Kumar and G. Pang, "Defect detection in textured materials using Gabor filters," *IEEE Trans. Ind. Appl.*, vol. 38, no. 2, pp. 425–440, Mar./Apr. 2002.

[34] A. Bodnarova, M. Bennamoun, and S. Latham, "Optimal Gabor filters for textile flaw detection," *Pattern Recog.*, vol. 35, pp. 2973–2991, 2002.

[35] A. Kumar and G. Pang, "Defect detection in textured materials using optimized filters," *IEEE Trans. Syst., Man, Cyber.-Part B: Cybern.*, vol. 32, no. 5, pp. 553–570, Oct. 2002.

[36] X. Xie and M. Mirmehdi, "TEXEMS: Texture exemplars for defect detection on random textured surfaces," *IEEE Trans. Pattern Anal. Mach. Intell.*, vol. 29, no. 8, pp. 1454–1464, Aug. 2007.

[37] P. T. Bourgeat, F. Meriaudeau, K. W. Tobin, Jr, and P. Gorria, "Patterned wafer segmentation," in *Proc. SPIE*, 2003, vol. 5132, pp. 36–44.

[38] N. G. Shankar and Z. W. Zhong, "Defect detection on semiconductor wafer surfaces," *Microelectron. Eng.*, vol. 77, pp. 337–346, 2005.

[39] C.-T. Su, T. Yang, and C.-M. Ke, "A neural network approach for semiconductor wafer post-sawing inspection," *IEEE Trans. Semiconductor Manuf.*, vol. 15, no. 2, pp. 260–266, May 2002.

[40] B. H. Khalaj, H. K. Aghajan, and T. Kailath, "Patterned wafer inspection by high resolution spectral estimation techniques," *Mach. Vision Appl.*, vol. 7, pp. 178–185, 1994.

[41] P. Xie and S.-U. Guan, "A golden-template self-generating method for patterned wafer inspection," *Mach. Vision Appl.*, vol. 12, pp. 149–156, 2000.

[42] S.-U. Guan, P. Xie, and H. Li, "A golden-block-based self-refining scheme for repetitive patterned wafer inspections," *Mach. Vision Appl.*, vol. 13, pp. 314–321, 2003.

[43] N. G. Shankar and Z. W. Zhong, "Improved segmentation of semiconductor defects using area sieves," *Mach. Vision Appl.*, vol. 17, pp. 1–7, 2006.

[44] K. Fukunaga and L. D. Hostetler, "The estimation of the gradient of a density function, with applications in pattern recognition," *IEEE Trans. Inform. Theory*, vol. 21, no. 1, pp. 32–40, Jan. 1975.

[45] D. Comaniciu and P. Meer, "Mean shift: A robust approach toward feature space analysis," *IEEE Trans. Pattern Anal. Mach. Intell.*, vol. 24, no. 5, pp. 603–619, May 2002.

[46] G. Hu, Q. Peng, and A. R. Forrest, "Mean shift denoising of point-sampled surfaces," *Visual Computer*, vol. 22, pp. 147–157, 2006.

[47] W. Liu, Y. Duan, K. Shao, and L. Zhang, "Image smoothing based on the mean shift algorithm," in *Proc. IEEE Int. Conf. Control Autom.*, Guangzhou, China, 2007, pp. 1349–1353.

[48] J. Wang, B. Thiesson, Y. Xu, and M. Cohen, "Image and video segmentation by anisotropic kernel mean shift," *Lecture Notes in Computer Science*, vol. 3022, pp. 238–249, 2004.
[49] W. Tao, H. Jin, and Y. Zhang, "Color image segmentation based on mean shift and normalized cuts," *IEEE Trans. Syst., Man Cybern.*, vol. 37, no. 5, pp. 1382–1389, Oct. 2007.
[50] B. Georgescu, I. Shimshoni, and P. Meer, "Mean shift based clustering in high dimensions: A texture classification example," in *Proc. IEEE Int. Conf. Comput. Vision*, Nice, France, 2003, vol. 1, pp. 456–463.
[51] M. F. A. Fauzi and P. H. Lewis, "Automatic texture segmentation for content-based image retrieval application," *Pattern Anal. Appl.*, vol. 9, pp. 307–323, 2006.
[52] J. F. Canny, "A computational approach to edge detection," *IEEE Trans. Pattern Anal. Mach. Intell.*, vol. PAMI–8, no. 6, pp. 679–698, NOV. 1986.

Du-Ming Tsai received the B.S. degree in industrial engineering from Tunghai University, Taichung, Taiwan, in 1981, and the M.S. and Ph.D. degrees in industrial engineering from Iowa State University, Ames, in 1984 and 1987, respectively.

From 1988 to 1990, he was a Principal Engineer at the Digital Equipment Corporation, Taiwan branch, where his work focused on process and automation research and development. Currently, he is a Professor of Industrial Engineering and Management at the Yuan-Ze University, Tao-Yuan, Taiwan. His research interests include automated visual inspection, object recognition, and texture analysis.

Jie-Yu Luo received the B.S. degree in industrial engineering and management from Aletheia University, Taipei, Taiwan, in 2007 and the M.S. degrees in industrial engineering and management from the Yuan-Ze University, Tao-Yuan, Taiwan, in 2009.

He is currently an Engineer with Chroma Ate Inc., Taiwan.